Absence of a Crystal Direction Regime in which Sputtering Corresponds to Amorphous Material

K. Schlueter
Max-Planck-Institut für Plasmaphysik, Boltzmannstrasse 2, D-85748 Garching, Germany and Fakultät für Maschinenwesen, Technische Universität München, D-85748 Garching, Germany

K. Nordlund
Department of Physics, University of Helsinki, P.O. Box 43, FIN-00014 Helsinki, Finland

G. Hobler
Institute of Solid-State Electronics, TU Wien, Gußhausstraße 25-25a, A-1040 Wien, Austria

M. Balden
Max-Planck-Institut für Plasmaphysik, Boltzmannstrasse 2, D-85748 Garching, Germany

F. Granberg and O. Flinck
Department of Physics, University of Helsinki, P.O. Box 43, FIN-00014 Helsinki, Finland

T. F. da Silva
Physics Institute of University of São Paulo, Rua do Matão 1371, 05508-090 São Paulo, Brazil

R. Neu
Max-Planck-Institut für Plasmaphysik, Boltzmannstrasse 2, D-85748 Garching, Germany and Fakultät für Maschinenwesen, Technische Universität München, D-85748 Garching, Germany

(Received 24 July 2020; accepted 7 October 2020; published 23 November 2020)

Erosion of material by energetic ions, i.e., sputtering, is widely used in industry and research. Using experiments and simulations that, independently of each other, obtain the sputter yield of thousands of individual grains, we demonstrate here that the sputter yield for heavy keV ions on metals changes as a continuous function of the crystal direction. Moreover, we show that polycrystalline metals with randomly oriented grains do not sputter with the same yield as the amorphous material. The key reason for this is attributed to linear collision sequences rather than channeling.

DOI: 10.1103/PhysRevLett.125.225502

The effect of the crystal lattice on material properties is a multifarious topic [1–12]. In applications, it may be employed to advantage, or, at least, it must be controlled. In general, the crystal lattice has an impact on many material properties; however, often only the low-index surfaces are investigated [13–18]. Therefore, a systematic study is highly desirable for characterizing properties such as sputtering [19,20] over many different crystal orientations.

Widely used sputter simulation programs such as TRIM [21] or SDTrimSP [22] assume an amorphous target; i.e., the crystal lattice structure is completely ignored [23,24]. Often, the sputter yield of a polycrystalline sample is compared with simulations [25], and the texture of the sample is not taken into account, even though it is well established that polycrystalline samples often have a preferred crystal orientation at the surface [26,27] and the sputter yield is reduced for low-index surface orientations [14–17]. The underlying assumption is that either the average over all directions corresponds to amorphous material [24,28] or there is a wide range of "random" crystal directions for which the yield is the same as in amorphous material.

This assumption is likely due to an assumed analogy to ion implantation. There, the projected ion range usually varies very little away from the major channeling directions. This is illustrated in Fig. 1(a), which shows an inverse pole figure (IPF) of the projected range of 30 keV Ga in single-crystalline W. An IPF is a stereographic projection of crystal directions. In cubic systems, due to symmetry the

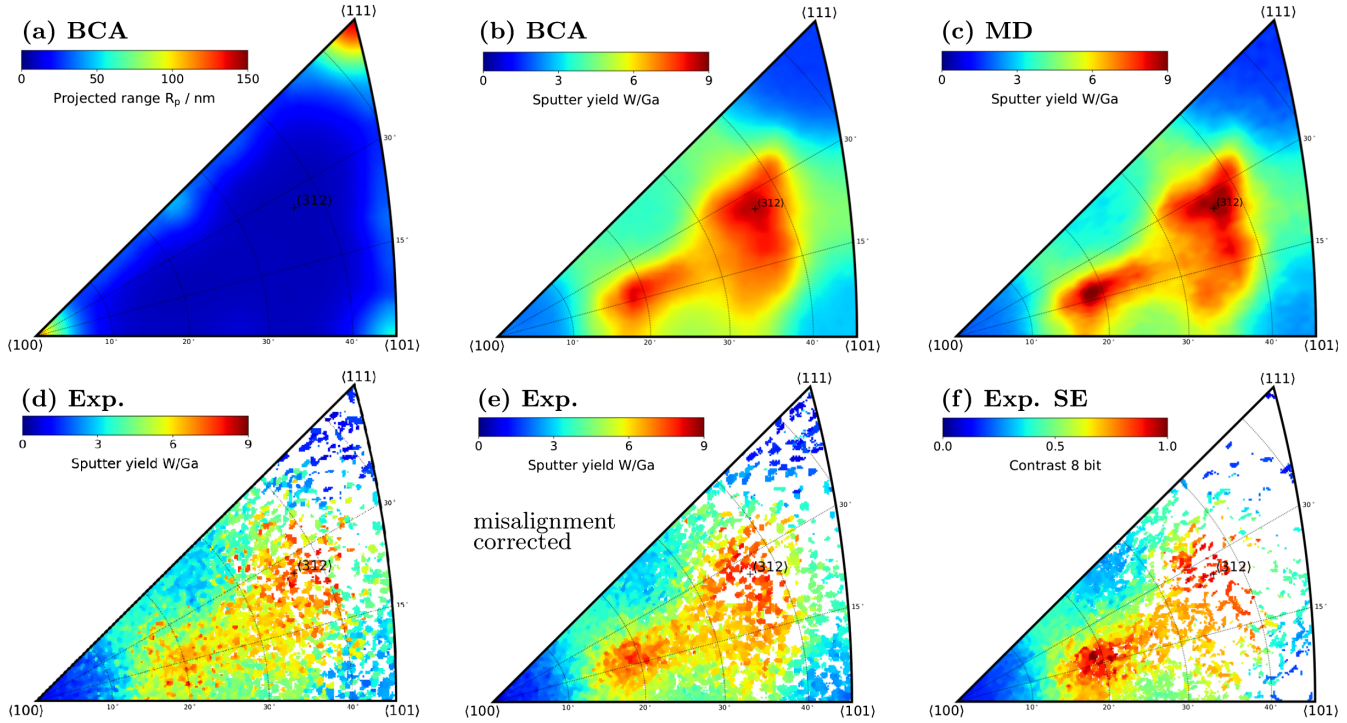

FIG. 1. IPFs for 30 keV Ga bombardment of W: (a) BCA simulations of the projected range of Ga; (b) BCA simulations of the sputter yield; (c) MD simulations of the sputter yield; (d) experimental sputter yield from four individual measurements; (e) experimental data of (d) corrected by rotation matrix multiplication according to PCA; (f) secondary electron emission. The white areas in the triangles in (d)–(f) represent crystal orientations for which no grains exist in the measured area.

triangle between ⟨001⟩, ⟨101⟩, and ⟨111⟩ represents the whole angular space. Figure 1(a) shows simulation results obtained with the binary collision approximation (BCA) code IMSIL [29]. The projected ranges are color coded based on an array of 46×46 implantation simulations for surface orientations covering the orientation triangle. For further details of the simulations, see Supplemental Material [30].

BCA simulations of single-crystal sputtering have been performed in the past [47–49] but only for selected surface orientations. In Fig. 1(b), we show an IPF for the sputter yield obtained by the same IMSIL simulations as used for Fig. 1(a). The ⟨100⟩ and ⟨111⟩ directions have the lowest sputter yield, while they have the largest projected range. However, in contrast to the projected range, the sputter yield changes continuously with crystal orientation, and there is no extended region where it is approximately constant.

In the following, we corroborate this result by molecular dynamics (MD) simulations and experiments using electron backscatter diffraction (EBSD) and scanning electron microscopy (SEM).

For the MD simulations, we developed a new approach to obtain sputter yields for arbitrary crystal orientations with the program MDRANGE, which is based on the recoil interaction approximation (RIA) [50,51]. In principle, MD simulations of the full development of collision cascades (which automatically include heat spike effects [52–56]) could provide the crystal direction dependence of sputtering. However, each full MD simulation is time consuming, and, to get a statistically reliable value for the sputter yield in a single direction, thousands of impacts are needed. Moreover, for obtaining IPFs, easily over thousands of directions are needed. These calculations are computationally prohibitive for full MD simulations. Therefore, MD simulations were performed on two levels. First, the crystal-direction dependence of the energy transfer to recoils in the top 2 nm of the surface of tungsten was simulated for all crystal directions using MDRANGE. Second, full MD cascade simulations using the PARCAS code [57–59] were performed of eight crystal directions to correlate energy to recoils with the sputter yield [30]. The result illustrates a linear dependence of the sputter yield on the energy to recoils within the statistical uncertainty (see Fig. S3 [30]). The slope of the linear regression obtained from the PARCAS simulations is used to translate the energy to recoils determined by MDRANGE to sputter yield in an IPF, which is shown in Fig. 1(c). Note the almost perfect agreement between MD and BCA results [Figs. 1(c) and 1(b), respectively].

Most previous experimental studies have investigated the sputter yield for some specific low-index crystal orientations only, and some others have measured sputter yield for a few additional orientations [14–17]. To go beyond this

standard approach, in this work we utilize recent developments in the EBSD technique that allow measuring and generating orientation maps of a polycrystalline sample in a reasonable time [60]. EBSD has been used to study dislocations [61], deformation structures within grains [62], or the crystal-dependent-oxidation behavior [63,64].

EBSD has previously been applied to examine sputter yields for 25 keV Ga bombardment of Mo [65] yet only for a few surface orientations. More recently, Nagasaki *et al.* have studied 4 keV Ar bombardment of polycrystalline Cu and Ni [66]. Although not discussed, the IPFs shown in that paper indicate a smooth variation of the sputter yield with surface orientation. However, their results have been smoothed due to the relative scarcity of the data, while our raw data have been sharpened by rotation matrix multiplication as described later.

For obtaining the experimental data, hot-rolled polycrystalline tungsten samples were recrystallized to achieve a grain size of around 10 μm. The samples were polished to achieve flat surfaces with height differences between the grains of less than 50 nm. The tungsten samples were sputtered by focused Ga ion beam (FIB) at 30 keV. The grains with the lowest sputter yield have an erosion of around 150 nm, and grains with the highest sputter yield have an 8 times higher erosion, which is measured with a confocal laser scanning microscope (CLSM). Between the sputter experiment and the height measurement, EBSD measurements were performed for determining the crystal orientation. The data of the orientation map and the height data were merged with a PYTHON tool, which was introduced and applied to grain-orientation-dependent oxidation in Ref. [64]. The height data were transformed to sputter yields by using the fluence and the atomic density of the target. Because of the well-known rectangular area irradiated by the scanning FIB, there is a well-defined reference level outside of the sputtered area, and the sputtered depth of each grain is accurately determined. At the end, the sputter yields of ten thousand single-crystal grains from four individual experiments were evaluated for the presented data. These results are visualized in the IPF shown in Fig. 1(d). Note that several grains correspond to each pixel, which represents one crystal direction. Therefore, the median of the sputter yields is reported for each pixel.

The huge data amount opens up the possibility for detailed analysis. A principal component analysis (PCA) is applied on the experimental data [67], to correct a possible misalignment error by the sample mounting or ion beam. A PCA captures the highest variation of the data in a lower dimension, here the IPF. An IPF includes all lattice symmetries and reduces the number of dimensions from three Euler angles to two independent variables characterizing one direction. When the direction is aligned with the ion beam, the highest variation of the data is kept in a lower dimension, because a rotation of the crystal lattice around the ion beam axis does not change the sputter yield; respectively, the ion beam faces the same crystal lattice in every rotation angle. On the EBSD data, rotation matrix multiplications result in a new arrangement of sputter yields in the IPF and the arrangement with the highest variation is desired [Fig. 1(e)].

The PCA was performed on each sputter experiment separately to compensate for the misalignment due to sample mounting or the positioning of the scan area of the FIB beam. The error of around 2° was corrected by rotation matrix multiplication. The resulting IPF shown in Fig. 1(e) is much clearer than that of the raw data [Fig. 1(d)]. The difference shows that the method is very sensitive to the misalignment error, and, in contrast to common assumptions, errors of the order of 1° have a significant impact on the data evaluation. Vice versa, the accuracy of the impact angle detection of the ions is better than 1° (Figs. S11 and S12 [30]).

Comparison of the experimental and simulated data [Figs. 1(b), 1(c), and 1(e)] shows excellent agreement of the dependence of the sputter yield on the crystal direction. It is emphasized that the simulations did not employ any fitting of parameters. The frequency distribution analysis of sputter yields shown in Fig. 2 confirms that the good agreement is not only visual. It also illustrates that the yields vary continuously and there is no single sputter yield value that would be much more common than the other, in contrast to the projected range. Moreover, the fact that the BCA and MD maximum sputter yields are similar indicates that heat spikes do not have a major contribution to sputtering under these irradiation conditions due to the very high melting point of W [54]. In addition, Fig. 2 shows the values of the sputter yield of amorphous and polycrystalline tungsten, 2.29 and 4.71 W/Ga, respectively, as

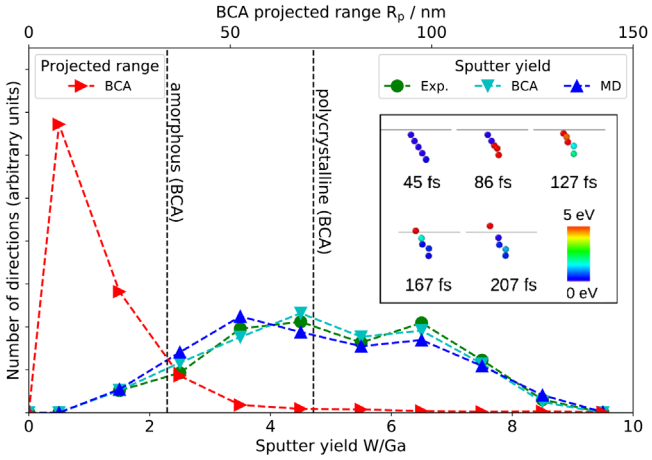

FIG. 2. Number of crystal directions versus sputter yield (green, cyan, and blue lines) and projected range (red line), assuming an isotropic distribution of surface orientations. The average sputter yield of polycrystalline and amorphous W as obtained by the BCA simulations is indicated by the vertical dashed lines. The inset shows an example of a linear collision sequence, which exists only in crystalline targets, observed in the MD simulations.

calculated with IMSIL. The discrepancy between the two will be discussed toward the end of the paper.

It is known that the sputter yield correlates with the secondary electron emission [68,69]. Therefore, secondary electron emission, caused by the Ga^+ FIB, was measured with the secondary electron detector of the microscope. The resulting grayscale image was merged with the crystal orientation image to visualize in an IPF, which is shown in Fig. 1(f). The distribution of the secondary electron yield versus the crystal orientation matches the experimental, MD, and BCA sputter yields very well. This demonstrates that secondary electron emission has a linear dependence on the sputter yield over thousands of data points (see Fig. S8 [30]).

In addition, the Ga implantation due to the crystal orientation was investigated. For that purpose, energy dispersive x-ray spectroscopy (EDX) measurements of the sputtered surface were performed, and the data were merged with the orientation data with the same PYTHON tool as used for the CLSM data [64]. The resulting IPF (Fig. S9 [30]) shows high Ga contents around low-index crystallographic directions where the projected range is large and the sputter yield small. This is to be expected, since both features make it more difficult to remove the implanted ions from the target.

For a detailed investigation of the depth distribution of the channeled Ga ions, FIB-prepared cross sections were made on low- and high-index surfaces for comparing them and verifying the Ga content with EDX. At the surface, the Ga content was around 20 at% in the ⟨100⟩ and ⟨111⟩ surface orientation. In contrast, at the high-index surfaces, the Ga content was below the detection limit of the EDX. Also, Ga was found down to about 350 nm below the surface in the ⟨100⟩ and ⟨111⟩ surface orientation. This result is in excellent agreement with MDRANGE and IMSIL simulations, whose electronic stopping power models have been calibrated with independent experimental [70] and theoretical data [71]. They show a maximum range of about 370 nm for these orientations.

These consistent and accurate experimental results, together with the BCA and MD simulations, convincingly show that there are no extended angular regions with almost constant sputter yield. To support the generality of this conclusion, we have in addition performed BCA simulations for 3 and 300 keV Ga bombardment with qualitatively similar results (see Fig. S1 [30]). In addition, measurements of the dependence of the sputter yield of Cu on the ion incidence angle for various ion beam conditions [14,15,28,72] may be interpreted as the superposition of a crystal orientation effect similar to that found in the present work and the incidence angle dependence of the sputter yield that is also present for amorphous targets. Thus, our result does not seem to be restricted to heavy ions and the bcc crystal lattice.

We briefly comment on the reasons why there is a continuous variation of the sputter yield with crystal orientation, while there are extended angular regions with almost constant projected ion ranges. Channeling, responsible for the increased projected range along low-index crystallographic directions, is the stable oscillation of trajectories in the open space between atomic rows or planes [73,74]. Thus, it takes full effect over an extended depth interval. In contrast, sputtering is a pronounced surface effect, which depends on various processes taking place in the near-surface region [72,75].

Finally, we comment on the difference between the average sputter yields of amorphous and polycrystalline tungsten as indicated in Fig. 2. It has long been known that so-called linear collision sequences [75,76] contribute to sputtering and cause spots in the angular distributions of the sputtered atoms. Since linear collision sequences can only occur in a crystalline material, the large difference in the sputter yields obtained by the BCA simulations using exactly the same physical models with only different target structures provides strong evidence that linear collision sequences contribute significantly to the sputter yield. Also, MD simulations comparing sputtering from amorphous and crystalline tungsten showed a similar difference and exhibited linear collision sequences; see the inset in Fig. 2. Details on the comparison between amorphous and crystalline material yields of the BCA and MD simulations are given in Supplemental Material [30].

In summary, new experimental and simulation approaches are developed for determining the crystal grain-orientation dependence of sputtering. Because of automated data collection processes, a huge amount of experimental data on sputtering can be collected, which, in turn, allows using filter techniques and new analysis methods to be applied on the dataset. This includes the optimization of the data due to the impact angle of the ions. In addition, this technique can be used to detect the impact angle of the ions to the sample surface with an accuracy better than 1°.

The newly developed approaches consistently show that for the system studied the low-index surfaces have more than a factor of 8 lower sputter yield than the high-index surfaces and that there is no continuous wide range of crystal directions that would correspond to the random material assumed in common Monte Carlo BCA codes. Moreover, detailed analysis of the atom collision sequences in the simulations showed that the reason for the large effects is that the physics of sputtering in polycrystalline nonamorphizing materials—such as common bulk elemental metals with high symmetric structure—is fundamentally different from that in amorphous materials.

This work has been carried out within the framework of the EUROfusion Consortium and has received funding from the Euratom research and training programme 2014–2018 and 2019–2020 under Grant Agreement No. 633053. The views and opinions expressed herein do not necessarily reflect those of the European Commission.

[1] W. Zhang and K. L. Turner, Sens. Actuators A **122**, 23 (2005).
[2] W. Utsumi, H. Saitoh, H. Kaneko, T. Watanuki, K. Aoki, and O. Shimomura, Nat. Mater. **2**, 735 (2003).
[3] L. Thomas, F. Lionti, R. Ballou, D. Gatteschi, R. Sessoli, and B. Barbara, Nature (London) **383**, 145 (1996).
[4] J. Goldberger, R. He, Y. Zhang, S. Lee, H. Yan, H.-J. Choi, and P. Yang, Nature (London) **422**, 599 (2003).
[5] T. Suwada, M. Satoh, K. Furukawa, T. Kamitani, T. Sugimura, K. Umemori, H. Okuno, Y. Endou, T. Haruna, R. Hamatsu *et al.*, Phys. Rev. Spec. Topics-Accelerators Beams **10**, 073501 (2007).
[6] A. Stognij, N. Novitskii, and O. Stukalov, Tech. Phys. Lett. **28**, 17 (2002).
[7] C. R. Giuliano, Appl. Phys. Lett. **21**, 39 (1972).
[8] W. Petasch, B. Kegel, H. Schmid, K. Lendenmann, and H. Keller, Surf. Coat. Technol. **97**, 176 (1997).
[9] D. O'kane and K. Mittal, J. Vac. Sci. Technol. **11**, 567 (1974).
[10] M. L. Swanson, J. Tesmer, and M. Nastasi, Channeling, in *Handbook of Modern Ion Beam Analysis*, edited by J. Tesmer, and M. Nastasi (Materials Research Society, Pittsburgh, PA, 1995), pp. 231–300.
[11] R. Simonton and A. F. Tasch, in Handbook of Ion Implantation Technology, edited by J. F. Ziegler (Elsevier, Amsterdam, 1992), pp. 119–221.
[12] M. Current, G. Hobler, Y. Kawasaki, and M. Sugitani, in *Proceedings of the 22nd International Conference on Ion Implantation Technology* (IEEE, New York, 2018), pp. 251–254.
[13] R. L. Davidchack and B. B. Laird, Phys. Rev. Lett. **94**, 086102 (2005).
[14] A. Southern, W. R. Willis, and M. T. Robinson, J. Appl. Phys. **34**, 153 (1963).
[15] H. E. Roosendaal, in *Sputtering by Particle Bombardment I*, edited by R. Behrisch (Springer, Berlin, 1981), pp. 219–256.
[16] D. E. Harrison, Jr., P. Kelly, B. J. Garrison, and N. Winograd, Surf. Sci. **76**, 311 (1978).
[17] G. K. Wehner, J. Appl. Phys. **26**, 1056 (1955).
[18] A. Litnovsky, Y. Krasikov, M. Rasinski, A. Kreter, C. Linsmeier, P. Mertens, B. Unterberg, U. Breuer, and T. Wegener, Fusion Eng. Des. **123**, 674 (2017).
[19] H. Gnaser, Energy and angular distributions of sputtered species, in *Sputtering by Particle Bombardment* (Springer, New York, 2007), pp. 231–328.
[20] G. Betz and K. Wien, Int. J. Mass Spectrom. Ion Process. **140**, 1 (1994).
[21] J. F. Ziegler, J. P. Biersack, and M. D. Ziegler, The stopping and range of ions in matter, SRIM, http://www.srim.org (2013).
[22] A. Mutzke, R. Schneider, W. Eckstein, and R. Dohmen, SDTrimSP: Version 5.00. ipp, report, (12/8), Max Planck-Institut fr Plasmaphysik, 2011.
[23] C. Lehmann and P. Sigmund, Phys. Status Solidi B **16**, 507 (1966).
[24] P. Sigmund, Phys. Rev. **184**, 383 (1969).
[25] R. Arredondo, M. Oberkofler, T. Schwarz-Selinger, U. von Toussaint, V. Burwitz, A. Mutzke, E. Vassallo, and M. Pedroni, Nucl. Mater. Energy **18**, 72 (2019).
[26] M. Hölscher, D. Raabe, and K. Lücke, Steel Res. **62**, 567 (1991).
[27] A. Manhard, G. Matern, and M. Balden, Practical Metallogr. **50**, 5 (2013).
[28] D. Onderdelinden, Can. J. Phys. **46**, 739 (1968).
[29] G. Hobler, Nucl. Instrum. Methods Phys. Res., Sect. B **96**, 155 (1995).
[30] See Supplemental Material at http://link.aps.org/supplemental/10.1103/PhysRevLett.125.225502 for details and additional results of simulations and experiments, which includes Refs. [31–46].
[31] C. Ebm and G. Hobler, Nucl. Instrum. Methods Phys. Res., Sect. B **267**, 2987 (2009).
[32] G. Hobler, D. Maciażek, and Z. Postawa, Phys. Rev. B **97**, 155307 (2018).
[33] J. F. Ziegler, J. P. Biersack, and U. Littmark, *The Stopping and Range of Ions in Solids* (Pergamon Press, New York, 1985).
[34] D. Onderdelinden, Appl. Phys. Lett. **8**, 189 (1966).
[35] O. S. Oen and M. T. Robinson, Nucl. Instrum. Methods **132**, 647 (1976).
[36] M. P. Allen and D. J. Tildesley, *Computer Simulation of Liquids* (Oxford University Press, Oxford, England, 1989).
[37] M.-C. Marinica, L. Ventelon, M. R. Gilbert, L. Proville, S. L. Dudarev, J. Marian, G. Bencteux, and F. Willaime, J. Phys. Condens. Matter **25**, 395502 (2013).
[38] A. E. Sand, J. Dequeker, C. S. Becquart, C. Domain, and K. Nordlund, J. Nucl. Mater. **470**, 119 (2016).
[39] X. Yi, A. Sand, D. Mason, M. Kirk, S. Roberts, K. Nordlund, and S. Dudarev, Europhys. Lett. **110**, 36001 (2015).
[40] A. E. Sand, J. Byggmästar, A. Zitting, and K. Nordlund, J. Nucl. Mater. **511**, 64 (2018).
[41] J. Delley, J. Chem. Phys. **92**, 508 (1990).
[42] DMol is a trademark of AccelRys. Inc.
[43] K. Nordlund, N. Runeberg, and D. Sundholm, Nucl. Instrum. Methods Phys. Res., Sect. B **132**, 45 (1997).
[44] J. Jussila, F. Granberg, and K. Nordlund, Nucl. Mater. Energy **17**, 113 (2018).
[45] D. Sprouster, R. Giulian, L. Araujo, P. Kluth, B. Johannessen, N. Kirby, K. Nordlund, and M. C. Ridgway, Phys. Rev. B **81**, 155414 (2010).
[46] L. Zhong, J. Wang, H. Sheng, Z. Zhang, and S. X. Mao, Nature (London) **512**, 177 (2014).
[47] M. T. Robinson, J. Appl. Phys. **54**, 2650 (1983).
[48] M. Hautala and J. Likonen, Phys. Rev. B **41**, 1759 (1990).
[49] A. V. Rogov, Y. V. Martynenko, N. E. Belova, and V. I. Shulga, Radiat. Eff. Defects Solids **166**, 894 (2011).
[50] K. Nordlund, F. Djurabekova, and G. Hobler, Phys. Rev. B **94**, 214109 (2016).
[51] K. Nordlund, Comput. Mater. Sci. **3**, 448 (1995).
[52] H. M. Urbassek and J. Michl, Nucl. Instrum. Methods Phys. Res., Sect. B **22**, 480 (1987).
[53] K. T. Waldeer and H. M. Urbassek, Nucl. Instrum. Methods Phys. Res., Sect. B **73**, 14 (1993).
[54] K. Nordlund, K. O. E. Henriksson, and J. Keinonen, Appl. Phys. Lett. **79**, 3624 (2001).
[55] S. Bouneau, A. Brunelle, S. Della-Negra, J. Depauw, D. Jacquet, Y. Le Beyec, M. Pautrat, M. Fallavier, J. Poizat, and H. Andersen, Phys. Rev. B **65**, 144106 (2002).

[56] G. Greaves, J. Hinks, P. Busby, N. Mellors, A. Ilinov, A. Kuronen, K. Nordlund, and S. Donnelly, Phys. Rev. Lett. **111**, 065504 (2013).
[57] PARCAS Computer code, available open source at https://gitlab.com/acclab/parcas/.
[58] K. Nordlund, M. Ghaly, R. S. Averback, M. Caturla, T. D. de La Rubia, and J. Tarus, Phys. Rev. B **57**, 7556 (1998).
[59] M. Ghaly, K. Nordlund, and R. S. Averback, Philos. Mag. A **79**, 795 (1999).
[60] J. Goulden, P. Trimby, and A. Bewick, Microsc. Microanal. **24**, 1128 (2018).
[61] W. Pantleon, Scr. Mater. **58**, 994 (2008).
[62] W. He, W. Ma, and W. Pantleon, Mater. Sci. Eng. A **494**, 21 (2008).
[63] K. Schlueter and M. Balden, Int. J. Refract. Met. Hard Mater. **79**, 102 (2019).
[64] K. Schlueter, M. Balden, and T. da Silva, Int. J. Refract. Met. Hard Mater. **88**, 105189 (2020).
[65] H. S. Huang, C. H. Chiu, I. T. Hong, H. C. Tung, and F. S. S. Chien, Mater. Charact. **83**, 68 (2013).
[66] T. Nagasaki, H. Hirai, M. Yoshino, and T. Yamada, Nucl. Instrum. Methods Phys. Res., Sect. B **418**, 34 (2018).
[67] T. A. Runkler, *Data Analytics: Models and Algorithms for Intelligent Data Analysis* (Springer, New York, 2016).
[68] Y. Stark, R. Frömter, D. Stickler, and H. P. Oepen, J. Appl. Phys. **105**, 013542 (2009).
[69] R. Franklin, E. Kirk, J. Cleaver, and H. Ahmed, J. Mater. Sci. Lett. **7**, 39 (1988).
[70] L. Eriksson, J. A. Davies, and P. Jespersgaard, Phys. Rev. **161**, 219 (1967).
[71] A. E. Sand, R. Ullah, and A. A. Correa, npj Comput. Mater. **5**, 43 (2019).
[72] V. Yurasova and V. Eltekov, Vacuum **32**, 399 (1982).
[73] J. Lindhard, *Influence of Crystal Lattice on Motion of Energetic Charged Particles*, Matematisk-fysiske Meddelelser Vol. 34 (The Royal Danish Society of Sciences, København (Copenhagen), 1965).
[74] G. Hobler, Radiat. Eff. Defects Solids **139**, 21 (1996).
[75] P. Sigmund, Thin Solid Films **520**, 6031 (2012).
[76] M. T. Robinson, in *Sputtering by Particle Bombardment I*, edited by R. Behrisch (Springer, Berlin, 1981), pp. 73–144.

Supplemental material to "Absence of a Crystal Direction Regime in which Sputtering Corresponds to Amorphous Material"

K. Schlueter
Max-Planck-Institut für Plasmaphysik, Boltzmannstr. 2, D-85748 Garching, Germany and Fakultät für Maschinenwesen, Technische Universität München, D-85748 Garching, Germany

K. Nordlund
Department of Physics, P.O. Box 43, FIN-00014, University of Helsinki, Finland

G. Hobler
Institute of Solid-State Electronics, TU Wien, Gußhausstraße 25-25a, A-1040 Wien, Austria

M. Balden
Max-Planck-Institut für Plasmaphysik, Boltzmannstr. 2, D-85748 Garching, Germany

F. Granberg and O. Flinck
Department of Physics, P.O. Box 43, FIN-00014, University of Helsinki, Finland

T.F. da Silva
Physics Institute of University of São Paulo - Rua do Matão 1371, 05508-090 São Paulo, Brazil

R. Neu
Max-Planck-Institut für Plasmaphysik, Boltzmannstr. 2, D-85748 Garching, Germany and Fakultät für Maschinenwesen, Technische Universität München, D-85748 Garching, Germany

(Dated: November 25, 2020)

I. DETAILS AND ADDITIONAL RESULTS OF THE BCA SIMULATIONS

A. Simulation details

The binary collision approximation (BCA) simulations have been performed with the IMSIL code. IMSIL has originally been developed for the simulation of ion implantation in silicon [1], and has been augmented over the years for other crystal systems and to allow sputtering simulations [2, 3]. For the present work, the universal ZBL interatomic potential [4] and a planar surface potential with a surface binding energy equal to the heat of sublimation (8.68 eV/atom) have been used. Collisions up to an impact parameter of 3 Å were taken into account. The average electronic stopping power has been taken to be equal to that of SRIM-2013 [5]. For the impact parameter dependence, the Oen-Robinson model [6] has been adapted:

$$\Delta E_e = \frac{S_e}{2\pi a^2} \exp\left(-\frac{r_0}{a}\right). \quad (1)$$

Here, S_e denotes the electronic stopping power, r_0 the distance of closest approach in the collision, and a a screening length. The latter has been fitted to experimental data [7] on the penetration of ions along channeling directions in W: $a = 5\,a_{\mathrm{ZBL}}$ for Ga, taken as the average between values obtained for Cu and Kr ions, and $a = 4.5\,a_{\mathrm{ZBL}}$ for W ions. a_{ZBL} denotes the screening length of the interatomic potential.

All simulations have been performed, like in the experiments, for perpendicular incidence of the ions. The crystallographic directions of the surface normal have been determined for each simulation from their stereographic projections, which were chosen on a regular 46×46 grid covering the [001], [101], and [011] directions. 10000 ion impacts have been simulated for each surface orientation, resulting in statistical errors of less than 1% for the projected range and less than 3% for the sputter yield.

In IMSIL, a polycrystalline target is simulated by randomly rotating the crystal coordinate system before each ion impact. For an amorphous target, free flight paths are chosen according to an exponential distribution with a mean value as to reflect the atomic density of W. Near to the surface, collision partners are generated like in the bulk, but collisions are abandoned when the target atom is found to lie outside the assumed surface.

All models and model parameters are fully consistent between crystalline-, polycrystalline-, and amorphous-target simulations. Unfortunately, BCA results sometimes depend significantly on the model parameters chosen. For instance, SDTrimSP [8] simulations with default parameters give more than a factor of two larger sputter yields than IMSIL. Careful analysis revealed that this is due to a much smaller maximum impact parameter used in SDTrimSP. Likewise, sputter yields obtained with SRIM [5] are much larger than those reported in the present work. Since the source code of SRIM is not accessible, it may only be speculated that this is due to the same reason. We conclude that the use of one and

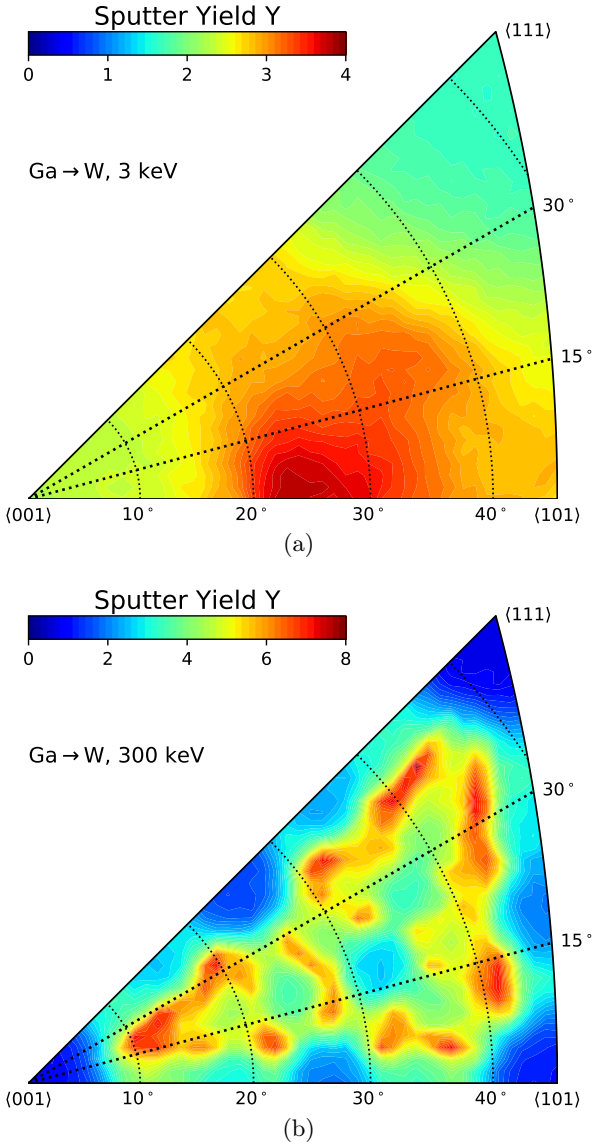

FIG. S1. IPFs for the W sputter yield as calculated by BCA simulations: (a) 3 keV Ga ions; (b) 300 keV Ga ions.

the same simulation program for all kinds of targets is essential for the validity of the present study.

B. Additional sputter yield results

Figure S1 shows inverse pole figures (IPFs) of the W sputter yield upon (a) 3 keV and (b) 300 keV Ga bombardement. For comparison, results for 30 keV Ga ions were shown in Fig. 1(b) of the main paper. The richness of the features increases with energy. This is similar to IPFs for the projected range [9, 10]. No extended region away from the low-index crystallographic directions with approximately constant sputter yield is observed in all three cases.

The average sputter yields of amorphous and polycrystalline W are 1.23 and 2.57, respectively, for 3 keV, and 1.98 and 3.70, respectively, for 300 keV. In both cases the sputter yield of amorphous W is significantly below the sputter yield of polycrystalline W, confirming the result for 30 keV Ga presented in the main paper.

C. Linear collision sequences

Linear collision sequences are sequences of collisions that occur along low-index crystallographic directions [11]. When one target atom is recoiled approximately aligned with a low-index direction, it hits another atom, which is likely to be recoiled towards a third atom in that row, and so on. In such a collision sequence, energy is transferred more efficiently than by the motion of a single recoil which loses energy to the surrounding atoms. A large fraction of the collisions in linear collision sequences are replacement collisions [11], i.e., the incoming atom stops while the recoil is set into motion. Therefore, replacement collisions are correlated with linear collision sequences.

Figure S2 shows recoil range distributions generated by IMSIL. When replacement collisions receive no special treatment (lines labeled "w/o replacements"), the recoil range distributions in amorphous and polycrystalline W are comparable. When replacement collisions are treated as if the incoming atom moves on with the momentum of the recoil, thus, as if no new recoil is generated (lines labeled "with replacements"), the number of recoils with a range between 5 Å and 20 Å is drastically increased in case of the polycrystal, while it is hardly affected in the amorphous target. This means that there is a significant number of long replacement collision sequences in the crystal, while they occur only rarely in the amorphous target. With the reported correlation between replacement and linear collision sequences, it may be concluded that linear collision sequences are significant in the polycrystalline target. When a linear collision sequence intersects the surface, a sputtering event may occur. Linear collision sequences thus appear as a likely cause of the increased sputter yield of the polycrystal compared to the amorphous target.

II. DETAILS OF THE MD SIMULATIONS

A. Simulation details

We used classical molecular dynamics (MD) simulations on two levels: i) MD simulations of the full development of collision cascades to simulate sputtering by 30 keV Ga ions of W in a few crystal orientations, and ii) MD simulations in the recoil interaction approximation (RIA) of the energy deposition by Ga ions near the W surface as a function of crystal orientation [10], for several Ga ion energies.

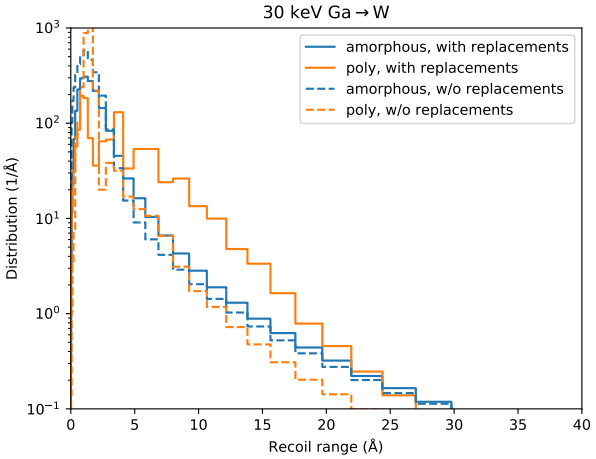

FIG. S2. Displacement distributions of W recoils in W caused by 30 keV Ga bombardment. Blue lines: amorphous W; orange lines: polycrystalline W. Considering stopped and recoiled atoms in a replacement collision as a single particle (solid lines) or as separate particles (dashed lines).

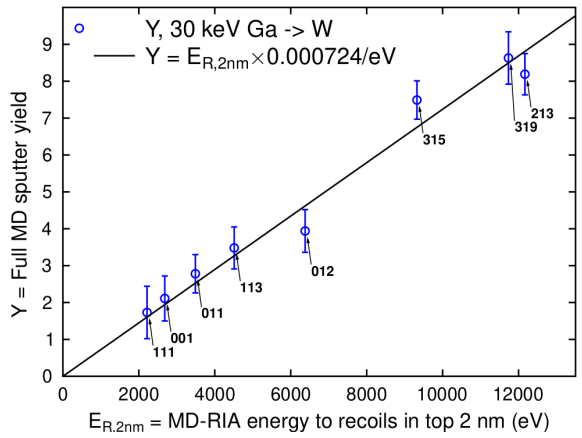

FIG. S3. Correlation between energy to recoils obtained from MD-RIA simulations and sputtering yields obtained indepently from full MD simulations. The slope of the linear regression is used to translate the MD-RIA energy to recoils into sputtering yields in the sputtering map over all directions.

In principle, simulation type (i) alone could be used to simulate the crystal direction dependence of sputtering. However, each full MD simulation is time-consuming by itself, and to get a statistically reliable value for the sputtering yield in a single direction, thousands of impacts are needed. To do a full map over thousands of directions is hence computationally prohibitive. The RIA simulation type (ii) is orders of magnitude more efficient than type (i) as only the ion is followed, making it practical to do a scan over all crystal directions.

The combination of approaches (i) and (ii) is further motivated by the Lindhard, Onderdelinden [12] and Sigmund [13] theories of sputtering, which state that the sputtering yield is proportional to the energy deposition at the surface. Hence, if this holds also under channeling conditions, one should be able to use the nuclear energy deposition simulations to get a channeling map similar to the experimental ones. To test whether the proportionality holds under the channeling condition, and also to obtain the proportionality between nuclear energy deposition and channeling condition, we carried out full MD simulations, simulation type (i), for a few selected channeling and non-channeling crystal directions. The directions were selected based on a channeling map, simulation type (ii) of 30 keV Ga ions in W.

The full MD sputtering runs, simulation type (i) were carried out using the classical molecular dynamics [14] code PARCAS [15], following basic surface simulation principles described in Ref. [16]. W was described with the well-tested Marinica interatomic potential [17–20], and the Ga-W interaction with a density-functional theory potential obtained with the DMol approach [21–23]. For this particular purpose of studying different surface orientations, we employed the approach from Ref. [24], in which an initially [001]-oriented crystal is first rotated with the Euler angles $(\theta, \phi, 0)$, after which a hemisphere is cut out and the surface is equilibrated to 300 K. The bombardment is carried out perpendicular to the rotated surface, from random starting positions near the center of the 16 nm radius hemisphere. The atoms in the outermost 0.3 nm atom layer of the hemisphere were fixed, and atoms 0.7 nm inside that were subject to temperature scaling. Tests with larger hemispheres showed that the 16 nm radius was sufficiently large for sputter simulations of 30 keV Ga ions in W. Atoms in the central collision region were simulated without any scaling, i.e., in the microcanonical NVE ensemble. For each orientation, 300 - 1000 ions were simulated to obtain a statistically meaningful sputtering yield Y. The statistical error of Y is obtained as the Gaussian 1σ error of the mean over the yields from all individual case yields. The Ziegler-Biersack-Littmark 1996 electronic stopping power [4] was implemented on all Ga ions and W recoils with a kinetic energy higher than 5 eV [25, 26] (without including the electronic stopping, the obtained sputtering yields were about a factor of 2 higher).

We tested that when electronic stopping is included, the sputtering yields are not very sensitive to the precise value of the threshold: changing the value of 5 eV to be a factor of 2 higher or lower lead to a change in the sputtering yields of $\lesssim 10\%$.

The MD-RIA calculations, simulation type (ii), were carried out with the MDRANGE code [25], very similarly to the channeling map simulations in Ref. [10]. To obtain the nuclear energy deposition near the surface, including a possible contribution from backscattered ions, the simulations were carried out for an infinite thickness sample, and the "energy to recoils" was recorded for the top 2 nm of the cell. Note that electronic stopping deposited by secondary and lower-order recoils is not included. We tested that using 1 nm or 4 nm gave the same trend in energy to recoils. We also tested recording the energy deposition only to recoils above 50 eV. This gave a scaling

between Y and E_R that was practically identical except for a different numerical prefactor.

B. Correlation of sputtering yield and surface energy deposition

The correlation between energy to recoils $E_{R,2nm}$ from MD-RIA and the sputtering yield from full MD simulations is shown in Fig. S3. The correspondence is excellent, and at least to a good first approximation linear (note that the error bars are 1σ ones, i.e., 1/3 of the data points should fall outside a correlation line). A fit of the simple linear equation $Y = AE_{R,2nm}$ $A = 0.000724 \pm 0.0000281/eV$ describes the correlation very well for 30 keV. This result essentially confirms that the Onderdelinden / Sigmund assumption of sputtering being proportional to deposited energy is also valid for channeling conditions.

Note that the full MD data also confirms independently the experiments and BCA simulations that the sputtering yield indeed has a strong dependence on crystal orientation. The difference between the minimum ($\langle 111 \rangle$ direction) and maximum ($\langle 315 \rangle$ direction) sputtering yields is about a factor of 5, in good agreement with the experimental results on large variation between yields.

Using the relation $Y = AE_{R,2nm}$ we can now recalculate the energy deposition channeling map into a simulation sputtering yield map. This comparison is shown in the main paper Fig. 1. The correspondence between experiment and simulation is remarkably good. The angular dependence of sputtering is practically indistinguishable.

C. Amorphous sample and linear collision sequences

As in the BCA simulations, we examined also in the MD simulations whether the sputtering yield and mechanism differ between an amorphous and crystalline material.

Although pure bulk elemental metals cannot be made amorphous experimentally (it is possible to make them on the nanoscale [27, 28]), in MD simulations it is possible to synthesize metastable amorphous metals by using faster quench rates that those is experimentally achievable. We created amorphous W by melt-quenching. A small cubic sample of initial size 4 nm with 4088 atoms (corresponding to the density of crystalline W) was heated to 10000 K and cooled down to 300 K with quench rates between 0.1 - 0.005 K/fs, with constant volume and periodic boundary conditions in all dimensions. After 300 K was reached, the cell was still simulated for 100 ps at constant temperature. Monitoring the potential energy and pair correlation function showed that quench rates in the range 0.005 - 0.02 K/fs gave cells with practically identical final potential energy and pair correlation function. One of the 0.01 K/fs cells was chosen as the model amorphous cell. This was then relaxed another time at 300 K using also pressure control to relieve the pressure left in the cell. The final a-W structure thus obtained had a potential energy of -8.494 eV/atom and a cell size of $4.016 \times 4.018 \times 4.022$ nm. This gives an atomic density of 63.0 atoms/nm^3, 1.4% lower than the density of 63.9 atoms/nm^3 for crystalline W in the same interatomic potential at 300 K. This model a-W cell was then used for MD-RIA calculations of the energy to recoils and repeated to give hemispherical cells for the full MD simulations.

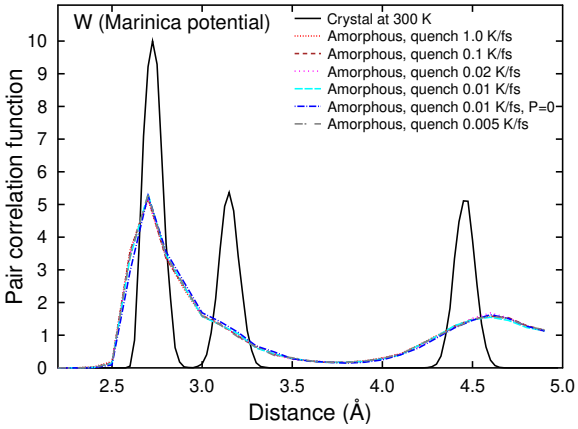

FIG. S4. Pair distribution functions for amorphous W obtained with different cooling rates. Also shown is the distribution function for crystalline W at 300 K and the distribution function for the final cell after relaxation to 0 pressure

Sputtering of a-W by 30 keV Ga was then simulated otherwise identically to the simulations in crystalline materials. The simulations gave a sputtering yield of 3.9 ± 0.4, while the MD-RIA simulations gave a surface energy deposition of 7650 eV in the top 2 nm. This can be compared with the values of the [315] crystalline surface, which had a sputtering yield of 7.5 ± 0.5 for a surface energy deposition of 9300 eV. In other words, in the MD simulations the amorphous material has a clearly lower sputtering yield per energy deposition than the crystalline one, well in line with the BCA result.

We also analyzed the reason to the lower energy deposition by comparing the MD simulations of 30 keV Ga irradiation of a-W in detail with simulations of the [315] and [012] surface, which have similar energy deposition. Analysis of individual events showed that the crystalline [315] direction simulation cell had much more high-yield events than the amorphous and these were for cases where the ion had stopped in the first few nm of the cell, see Fig. S5.

The 30 keV cascades are, however, rather complex and difficult to analyze. Hence we also set up model simulations at lower energies, that allow for more detailed analysis and faster collection of data with good statis-

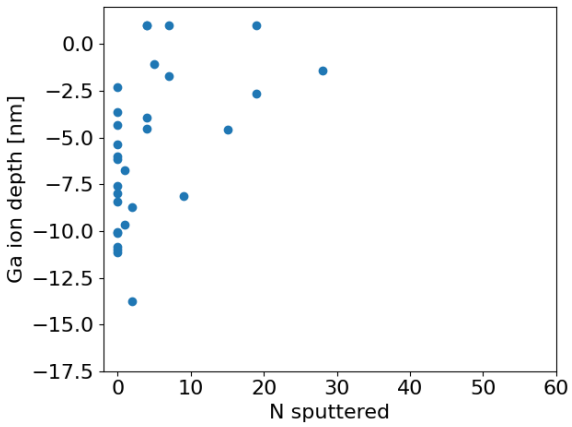

(a)

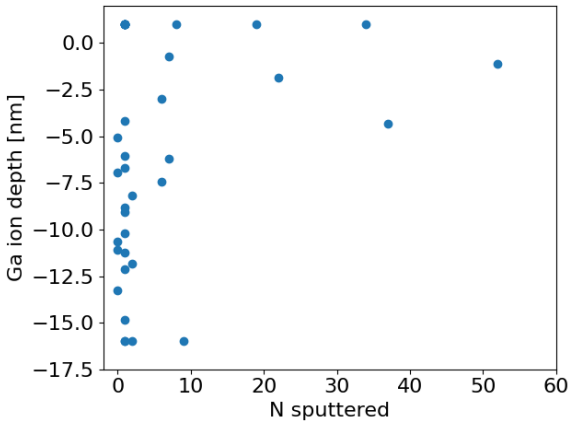

(b)

FIG. S5. Relation between sputtering yield and final Ga ion depth for individual events for (a) Amorphous W and (b) Crystalline W with [315] surface normal. The data points above 0 nm are for Ga ions that were reflected.

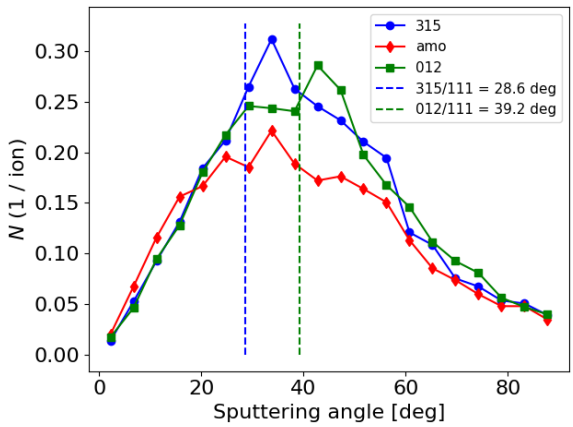

(a)

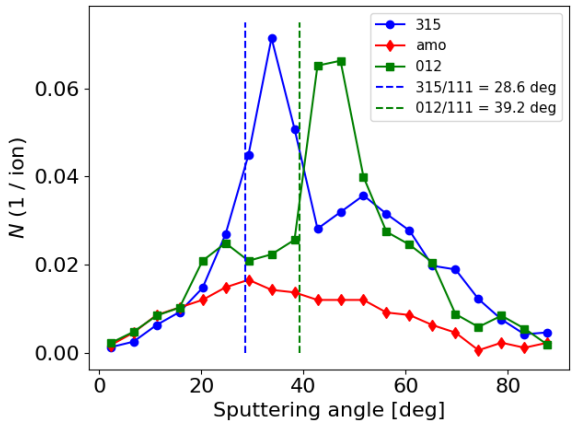

(b)

FIG. S6. Fractional sputtering yields as a function of the outgoing angle of the sputtered particles for 5 keV W recoils, (a) recoils in top surface layer (b) 1 nm deep, for a crystalline cell with [315] and [012] surface orientations and an amorphous W cell.

tics. We chose to simulate 5 keV and 7.5 keV W recoils chosen randomly from either the first monolayer (0 nm deep) or from a depth of 1 nm. The recoils were directed downwards at a random angle between 0° and 40° off-normal, to correspond to a typical case of the Ga ions giving a recoil energy to W sample atoms. The simulations were carried out in identical configurations for the amorphous, [315] and [012] surfaces.

The simulations showed that in all cases, the crystalline surfaces had larger sputtering yields than the amorphous ones. Note that because the initial recoil energies where the same, this rules out that the difference is due to differences in surface layer energy deposition by the ion. Moreover, the recoils starting 1 nm deep showed a much larger difference than the ones starting at 0 nm. This indicates that in the current case, the key difference does not stem from the first monolayer. It was early on suggested that differences in atom binding energy due to atom positioning at the surface could cause marked differences in sputtering [29] and recent simulations have indeed shown that this can be the case for $\lesssim 1$ keV Ar irradiation of W [24]. However, in the current case of higher energies, this clearly is not the dominant effect.

To understand the origin of the increased sputtering on the crystalline surfaces, we analyzed the outgoing angle of sputtered atoms. Results for this are shown in Fig. S6 for the case of 5 keV recoils (7.5 keV gave very similar results and are not shown). For the recoils in the top layer, the angular dependence is smooth. However, for the recoils from 1 nm deep, there is a distinct peak around 35° off-normal for the crystalline surface. This is strongly indicative of sputtering due to linear collision sequences in the ⟨111⟩ direction in a BCC metal. The angle between the ⟨111⟩ and ⟨315⟩ directions is about 29°, and indicated with the dashed vertical line in the figures. Looking more closely at the event resulting in W atoms sputtered in the 29° angle, these linear collision sequences could be observed for the [315] surface orientation. Two examples on the energy transfer in this linear collision sequence

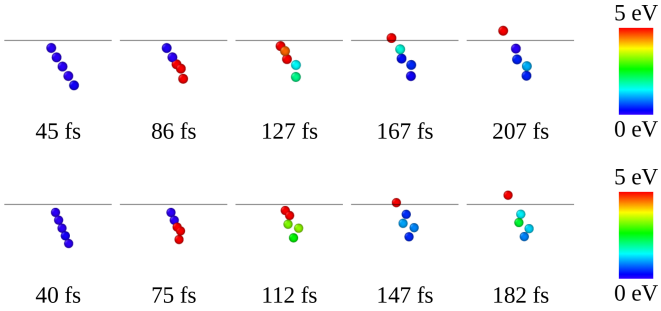

FIG. S7. Two examples of the linear collision sequence leading to a sputtering event for the [315] surface orientation. The color coding is according to the kinetic energy of the atoms.

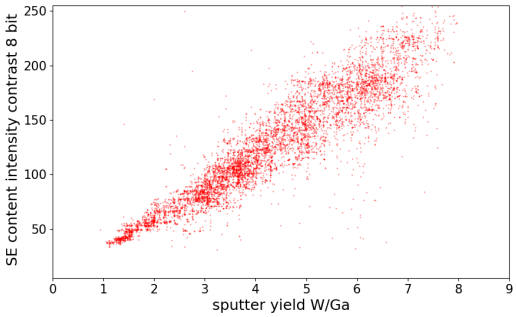

FIG. S8. Secondary electron emission versus the sputter yield is shown. A linear dependency between the sputter yield and the secondary electron emission.

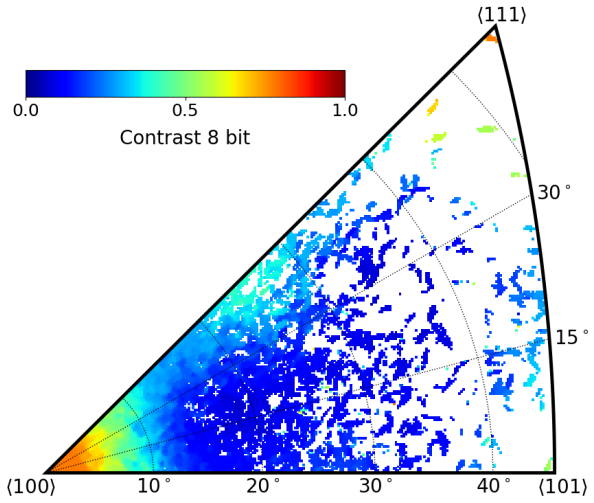

FIG. S9. Distribution of the EDX Ga intensity map versus the crystal orientation after sputtering with a 30 keV Ga ion beam of a polycrystalline tungsten bulk sample. The EDX measurements were performed with a 5 keV electron beam.

can be seen in Fig. S7. The likely reason that the peak is at a somewhat higher angle is that after an atom leaves the surface, interactions with the surface atoms steer the sputtered particles to slightly higher emission angles.

Hence, to summarize both, the BCA and MD simulations point to linear collision sequences being the main reason for higher sputtering yields at crystalline surfaces compared to amorphous ones.

III. EXPERIMENTAL DETAILS

A. Sample preparation and characterization

For obtaining the experimental data, hot rolled polycrystalline W samples of the purity of 99.97 wt% (Plansee SE, Austria) were recrystallized at 2000 K for 30 minutes under vacuum pressure below 10^{-7} mbar, which results in a typical grain size of 10 μm. The samples were grounded and electro-polished to achieve flat surfaces with height differences between the grains of less than 50 nm.

The samples were sputtered with a Ga focused ion beam (FIB) in an electron scanning microscope (FEI, Helios Nanolab 600). An electron backscatter diffraction (EBSD) detector (Oxford Instr., Symmetry) is attached to this microscope for measuring orientation maps of the sputtered areas. Using one machine reduces systematical errors, e.g., of mounting the sample under a certain angle. After the sputter experiment, the post-characterization includes EBSD, the measurement of the three dimensional surface profile of the samples using a confocal laser scanning microscope (CLSM) (Olympus, LEXT OSL4000), measurement of the Ga intensity with energy dispersive X-ray spectroscopy (EDX) (Oxford Instr., Ultim Extreme) and the secondary electron emission using the Everhart-Thornley detector of the SEM.

B. Secondary electrons

Areas presputtered with a 30 keV Ga ion beam were scanned again with a 30 keV Ga ion beam and an Everhart-Thornley detector was used to detect the secondary electron emission in each point. The contrast data was merged with EBSD data, evaluated and visualized as an inverse pole figure (IPF). The Everhart-Thornley detector was not calibrated to the absolute amount of secondary electrons. Therefore, only the differences in the secondary electron emission between many crystal orientations were evaluated. Since thousands crystal orientations are evaluated for secondary electron emission and the sputter yields, both data sets were correlated to each other as shown in Fig. S8. The figure shows a linear dependence between the sputter yield and the secondary electron emission.

C. EDX of Gallium

After the 30 keV Ga ion sputter experiment, the sputtered area was investigated with an EDX surface inten-

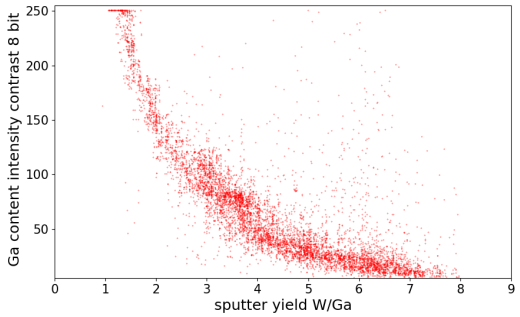

FIG. S10. Intensity of Ga from an EDX surface map versus the sputter yield.

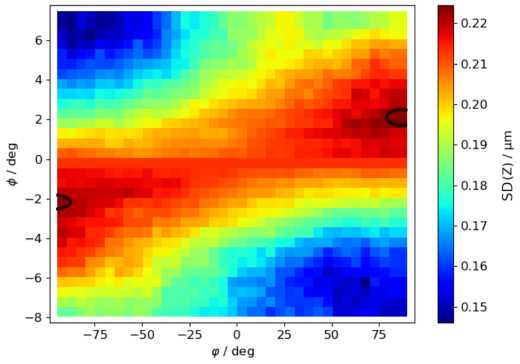

FIG. S11. Result of the principal component analysis (PCA). The highest standard derivation (SD) is by rotation angle of $\varphi = 80°$ and ϕ=2°. The area is marked with a black circle.

sity map. A quantification of these data is inaccurate, because every crystal orientation influences the penetration of the electron beam as well as the Ga distribution is far off being homogeneously distributed over the depth. Therefore, instead of the Ga content, the intensity map of the EDX data was used and merged with EBSD data. Afterwards, the data was evaluated and visualized in an IPF, which is shown in Fig. S9.

Since thousands of crystal orientations were evaluated for EDX data and the sputter yields, both data sets were correlated to each other as shown in Fig. S10. This figure shows an exponential dependence between the sputter yield and the gallium intensity of an EDX map.

D. Result of the PCA

Since thousands of single crystal grain sputter yields were measured, a principal component analysis (PCA) analysis was performed on the EBSD data. The crystal lattices were first rotated around the first Euler angle φ, second rotated around the second Euler angle ϕ and the standard derivation (SD) was determined of the sputter

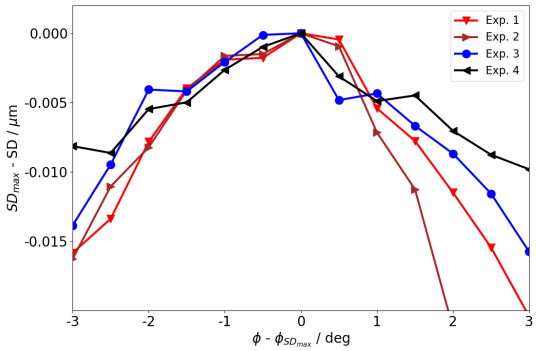

FIG. S12. Result of the principal component analysis (PCA). The highest standard derivation (SD) is compared to the impact angles ϕ of 4 different experiments.

yields of the IPF. Only the second rotation is responsible for the misorientation angle to the surface normal. A symmetry point is a rotation of +90° or -90° around the surface normal (first Euler angle φ). This is visible in Fig. S11. A rotation of $\varphi = 90°$ and $\phi = 2°$ is the same as a rotation of φ = -90° and ϕ = -2°. For clarification, the rotation of $\varphi = 90°$ and $\phi = 2°$ is in principal a rotation of 2° around the y axis of the sample coordinate system. Each of the four experiments were optimized with PCA and the data was corrected. Afterwards, all four experimental data sets were combined together. The correction has a big effect on the result as shown in the main paper. For the four sputter experiments the highest SD was found for ϕ_{max} = 0.5°, -1.5°, 2°, -4° and φ_{max} = -90°, -70°, 80°, 30°.

The correction by ϕ = -4° results from an obvious sample misalignment noticed after the experiment. The detection of the impact angle ϕ of the ions has an error of less than 1°, because the correction of the impact angles ϕ was significant and the result is closer to the simulation, which is shown in Fig. 1(e) of the main paper. In addition, Fig. S12 shows the evaluation to a fixed rotation angle φ, which includes the highest SD through the PCA analysis, e.g., in Fig. S11 $\varphi = 80°$. With a fixed rotation angle, the impact angle ϕ is plotted against the SD. If in Fig. S12 one of the four curves is shifted by 1°, it will be clearly off the others. This also shows that the impact angle ϕ can be evaluated better than 1° accuracy.

Due to the high sensitivity to the impact angle, the method is suitable for an ion direction detector.

[1] G. Hobler, Nucl. Instrum. Methods **B 96**, 155 (1995).
[2] C. Ebm and G. Hobler, Nucl. Instrum. Methods **B 267**, 2987 (2009).
[3] G. Hobler, D. Maciążek, and Z. Postawa, Phys. Rev. B **97**, 155307 (2018).
[4] J. F. Ziegler, J. P. Biersack, and U. Littmark, (Pergamon Press, New York, 1985).
[5] J. F. Ziegler, J. P. Biersack, and M. D. Ziegler, The stopping and range of ions in matter, SRIM: http://www.srim.org (2013).
[6] O. S. Oen and M. T. Robinson, Nucl. Instrum. Methods **132**, 647 (1976).
[7] L. Eriksson, J. A. Davies, and P. Jespersgaard, Phys. Rev. **161**, 219 (1967).
[8] A. Mutzke, R. Schneider, W. Eckstein, and R. Dohmen, Sdtrimsp: Version 5.00. ipp, report,(12/8), Max Planck-Institut für Plasmaphysik (2011).
[9] G. Hobler, Radiat. Eff. Def. Sol. **139**, 21 (1996).
[10] K. Nordlund, F. Djurabekova, and G. Hobler, Phys. Rev. B **94**, 214109 (2016).
[11] M. T. Robinson, in *Sputtering by Particle Bombardment I*, edited by R. Behrisch (Springer, Berlin, 1981) pp. 73–144.
[12] D. Onderdelinden, Appl. Phys. Lett. **8**, 189 (1966).
[13] P. Sigmund, Phys. Rev. **184**, 383 (1969).
[14] M. P. Allen and D. J. Tildesley, *Computer Simulation of Liquids* (Oxford University Press, Oxford, England, 1989).
[15] PARCAS Computer code, available open source at https://gitlab.com/acclab/parcas/.
[16] M. Ghaly, K. Nordlund, and R. S. Averback, Philo. Mag. A **79**, 795 (1999).
[17] M.-C. Marinica, L. Ventelon, M. R. Gilbert, L. Proville, S. L. Dudarev, J. Marian, G. Bencteux, and F. Willaime, Interatomic potentials for modelling radiation defects and dislocations in tungsten, J. Phys.: Condens. Matter **25**, 395502 (2013).
[18] A. E. Sand, J. Dequeker, C. S. Becquart, C. Domain, and K. Nordlund, Non-equilibrium properties of interatomic potentials in cascade simulations in tungsten, J. Nucl. Mater. **470**, 119 (2016).
[19] X. Yi, A. Sand, D. Mason, M. Kirk, S. Roberts, K. Nordlund, and S. Dudarev, EPL (Europhys. Lett.) **110**, 36001 (2015).
[20] A. E. Sand and J. Byggmästar and A. Zitting and K. Nordlund, Defect structures and statistics in overlapping cascade damage in fusion-relevant bcc metals, J. Nucl. Mater. **511**, 405701 (2018).
[21] J. Delley, J. Chem. Phys. **92**, 508 (1990).
[22] DMol is a trademark of AccelRys. Inc.
[23] K. Nordlund, N. Runeberg, and D. Sundholm, Repulsive interatomic potentials calculated using Hartree-Fock and density-functional theory methods, Nucl. Instr. Meth. Phys. Res. B **132**, 45 (1997).
[24] J. Jussila, F. Granberg, and K. Nordlund, Effect of Random Surface Orientation on W Sputtering Yields, Nucl. Mater. Energy **17**, 113 (2018).
[25] K. Nordlund, Computat. Mater. Sci. **3**, 448 (1995).
[26] K. Nordlund, M. Ghaly, R. S. Averback, M. Caturla, T. D. de La Rubia, and J. Tarus, Phys. Rev. B **57**, 7556 (1998).
[27] D. Sprouster, R. Giulian, L. Araujo, P. Kluth, B. Johannessen, N. Kirby, K. Nordlund, and M. C. Ridgway, Ion-irradiation-induced amorphization of cobalt nanoparticles, Phys. Rev. B **81**, 155414 (2010).
[28] L. Zhong, J. Wang, H. Sheng, Z. Zhang, and S. X. Mao, Formation of monatomic metallic glasses through ultrafast liquid quenching, Nature **512**, 177 (2014).
[29] C. Lehmann and P. Sigmund, Phys. Status Solidi B **16**, 507 (1966).